TU Delft

Delft University of Technology

Experimental Investigation of the Aerodynamic Performance of a Propeller at Positive and Negative Thrust and Power

Nederlof, R.; Ragni, D.; Sinnige, T.

DOI
10.2514/6.2022-3893

Publication date
2022

Document Version
Final published version

Published in
AIAA AVIATION 2022 Forum

Citation (APA)
Nederlof, R., Ragni, D., & Sinnige, T. (2022). Experimental Investigation of the Aerodynamic Performance of a Propeller at Positive and Negative Thrust and Power. In *AIAA AVIATION 2022 Forum* Article AIAA 2022-3893 (AIAA AVIATION 2022 Forum). American Institute of Aeronautics and Astronautics Inc. (AIAA). https://doi.org/10.2514/6.2022-3893

Important note
To cite this publication, please use the final published version (if applicable).
Please check the document version above.

Copyright
Other than for strictly personal use, it is not permitted to download, forward or distribute the text or part of it, without the consent of the author(s) and/or copyright holder(s), unless the work is under an open content license such as Creative Commons.

Takedown policy
Please contact us and provide details if you believe this document breaches copyrights.
We will remove access to the work immediately and investigate your claim.

This work is downloaded from Delft University of Technology.
For technical reasons the number of authors shown on this cover page is limited to a maximum of 10.

AIAA AVIATION Forum
June 27-July 1, 2022, Chicago, IL & Virtual
AIAA AVIATION 2022 Forum

10.2514/6.2022-3893

Check for updates

Experimental Investigation of the Aerodynamic Performance of a Propeller at Positive and Negative Thrust and Power

R. Nederlof*, D. Ragni† and T. Sinnige‡
Delft University of Technology, Delft, 2629 HS, Netherlands

The use of electric motors enables a more flexible operation of propellers compared to conventional combustion engines. One possible benefit is the easier operation at negative thrust, which could be beneficial for energy recovery, control purposes, and lower noise through steeper descents. By changing the pitch of the propellers and actively braking them, the torque and thrust are in the opposite direction compared to the conventional positive thrust conditions. The aerodynamic off-design operations at the blade section in this operational regime impact the blade loading. An experimental investigation was carried out to analyze the aerodynamic performance of a three-bladed propeller in both positive and negative thrust and power conditions. Next to the integral propeller forces, the slipstream was analyzed to obtain a better understanding of the physical phenomena that determine the performance in the negative thrust regime. Both stereoscopic PIV and a 5-hole probe were used to obtain the local velocity and total pressure distributions inside the slipstream for three different thrust settings. The results show that the negative thrust operation is dominated by stall on a large part of the blades, limiting the negative shaft power. The maximum energy-harvesting efficiency is obtained for a low pitch setting and was found to be about 11%. However, the energy-harvesting at low pitch settings comes at a cost of high negative thrust. For low negative thrust values, the propeller can actually harvest more energy at a higher pitch setting. The slipstream analyses showed an almost flat blade radial loading distribution in the negative thrust regime indicating sub-optimal blade performance and possible separation on the blade sections. The velocity field in the propeller slipstream showed a reduction in axial velocity and an opposite swirl direction compared to the positive thrust mode when the propeller was used to harvest energy.

Downloaded by TU DELFT on August 16, 2022 | http://arc.aiaa.org | DOI: 10.2514/6.2022-3893

Nomenclature

Roman Symbols

A	=	propeller disk area [m^2]	P	=	propeller power [W]
C_d	=	sectional drag coefficient [-]	P_C	=	power coefficient ($P/(\rho V_\infty^3 D_\mathrm{p}^2)$) [-]
C_l	=	sectional lift coefficient [-]	p	=	pressure [Pa]
C_P	=	power coefficient ($P/(\rho n^3 D_\mathrm{p}^5)$) [-]	Q	=	torque [Nm]
C_p	=	pressure coefficient [-]	Q_C	=	torque coefficient ($Q/(\rho V_\infty^2 D_\mathrm{p}^3)$) [-]
C_Q	=	torque coefficient ($Q/(\rho n^2 D_\mathrm{p}^5)$) [-]	q	=	dynamic pressure [Pa]
C_q	=	sectional torque coefficient [-]	R	=	propeller radius [m]
C_T	=	thrust coefficient ($T/(\rho n^2 D_\mathrm{p}^4)$) [-]	r	=	radial coordinate [m]
C_t	=	sectional thrust coefficient [-]	Re	=	Reynolds number [-]
c	=	chord of blade section [m]	T	=	thrust force [N]
D	=	drag force [N]	T_C	=	thrust coefficient ($T/(\rho V_\infty^2 D_\mathrm{p}^2)$) [-]
D_p	=	propeller diameter [m]	V	=	velocity [m/s]
J	=	advance ratio ($V_\infty/(nD_\mathrm{p})$) [-]	V_eff	=	effective velocity at blade section [m/s]
L	=	lift force [N]	X	=	streamwise coordinate [m]
M_tip	=	tip Mach number [-]	Y	=	horizontal coordinate [m]
n	=	propeller rotational speed [Hz]	Z	=	vertical coordinate [m]

*PhD Candidate, Flight Performance and Propulsion Section, Faculty of Aerospace Engineering, Kluyverweg 1; R.Nederlof-1@tudelft.nl
†Associate professor, Wind Energy Section, Faculty of Aerospace Engineering, Kluyverweg 1
‡Assistant professor, Flight Performance and Propulsion Section, Faculty of Aerospace Engineering, Kluyverweg 1; Member AIAA.

Copyright © 2022 by R. Nederlof, D. Ragni, and T. Sinnige. Published by the American Institute of Aeronautics and Astronautics, Inc., with permission.

Greek Symbols

α	=	angle of attack [°]	η_p	=	propeller efficiency (TV_∞/P) [-]
β	=	blade pitch angle [°]	η_t	=	turbine efficiency ($P/(TV_\infty)$) [-]
η_{eh}	=	energy-harvesting efficiency ($P/(\frac{1}{2}\rho V_\infty^3 A)$) [-]	ρ	=	air density [kg/m^3]

Subscripts

$0.7R$	=	at 70% blade radius	r	=	radial (velocity)
13	=	delta between hole 1 and 3 (5-hole probe)	s	=	static (pressure)
24	=	delta between hole 2 and 4 (5-hole probe)	t	=	tangential (velocity)
5	=	hole 5 (5-hole probe)	t	=	total (pressure)
a	=	axial (velocity)	∞	=	free stream

Downloaded by TU DELFT on August 16, 2022 | http://arc.aiaa.org | DOI: 10.2514/6.2022-3893

I. Introduction

The rapid growth of air traffic has exacerbated climate change and noise hindrance and the electrification of aircraft can help to reduce them. Despite the lower energy density of batteries compared to jet fuels, the increased design freedom associated with electric aircraft offers potential integration benefits, which can be exploited to improve the complete system performance [1, 2]. The use of electric motors makes it possible to use multiple smaller engines that are distributed over the aircraft with propellers as thrust-producing devices. One example of such an approach is the NASA X-57, on which distributed propellers along the leading edge can be used as means of high-lift augmentation, whereas they can be stowed during cruise to increase aerodynamic efficiency in this phase [3, 4]. At the same time, beneficial interactions between the propellers themselves or with the airframe can be exploited to improve the overall system performance, such as reduction in wing drag in the case of wingtip-mounted propellers [5]. Distributed propellers could also be used for control and stability or could be used as airbrake to steepen descent and hence reduce community noise. Furthermore, the propellers could be used as wind turbines to harvest energy during phases of the flight where energy input is not required, such as during descent [6]. This energy harvesting process may decrease the total energy required for the aircraft, depending on the flight mission. The Slovenian aircraft manufacturer Pipistrel tested the energy-harvesting performance of their Alpha Electro through real flight tests [7]. For the standard propeller design, only marginal energy savings were observed. However, for an improved blade design, where the energy-harvesting process was taken into account, better energy savings were reported. A 19% reduction in net energy consumption was observed compared to the original propeller. For this small trainer aircraft, the saved energy would result in a 27% increase in the possible number of traffic patterns [7].

In terms of the propeller operation, a distinction is made between three different modes. The first one is in which the propeller produces positive thrust and requires positive (input) power, which is referred to as the propulsive mode. The opposite mode of the propulsive mode is referred to as the energy-harvesting mode in this paper. In this mode, the propeller will produce negative thrust and negative (output) power and this operation is similar to a wind turbine. Then there is a mode in between, in which the thrust produced already is negative, while still a net power input is needed, and this is referred to as the braking mode. The aerodynamics of propellers in the energy-harvesting regime are drastically different than in the propulsive regime. In Fig. 1, the velocity triangles and blade forces of a propeller blade section are shown for the propulsive and energy-harvesting mode in Fig. 1a and Fig. 1b respectively. For the propulsive mode, there is a positive angle of attack (α) between the effective velocity (V_{eff}) and the chord line of the blade section, which results in positive lift and hence positive thrust. If the propeller is used to harvest energy, the forces on the blade sections are inverted, meaning there will be a drag (negative thrust) component instead of positive thrust and the torque is also in the opposite direction, even though the rotation direction remains unaltered. This negative torque component is what leads to energy-harvesting.

When the propeller generates negative thrust, it will not be operating in design conditions. The propeller blades are optimized for propulsive performance, meaning negative angles of attack are required for the highly cambered profiles to actually create the negative thrust and power. This means that the blade sections will be prone to stall conditions resulting in a poor performance and unsteady phenomena such as vibrations. An initial wind tunnel experiment performed by Sinnige et al. [8] revealed a maximum energy-harvesting efficiency of around 10%, which is significantly lower compared to the values reached by conventional wind turbines.

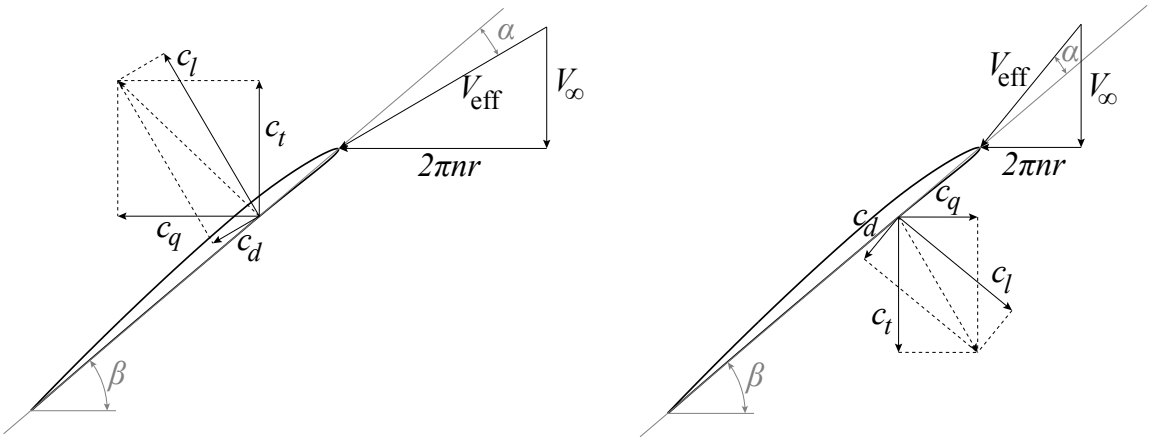

(a) Propulsive mode **(b) Energy-harvesting mode**

Fig. 1 Velocity triangles and blade forces of a blade section in both propulsive and energy-harvesting mode [8]

Downloaded by TU DELFT on August 16, 2022 | http://arc.aiaa.org | DOI: 10.2514/6.2022-3893

It was found that the aerodynamic performance of the highly cambered blade sections was limited due to stall on the blades [8, 9]. Possible redesign of the propeller blades could enhance the energy-harvesting efficiency, as was shown for the Alpha Electro [7], however, this should not compromise the propeller efficiency in cruise. The aerodynamics of both propellers and wind turbines are well understood when they are operating in their conventional regime. However, when the propeller is used as a wind turbine, the propeller blades will operate in off-design conditions. Detailed understanding of the flow around the blade sections and the slipstream characteristics behind the blades is still missing for these off-design conditions and design routines are unknown for energy-harvesting propellers. Due to the off-design operation of the propeller in energy-harvesting mode, conventional numerical tools seem to be unable to accurately predict the performance in this mode [10].

This paper focuses on the isolated propeller performance and the goal is to explain the physical phenomena that drive the performance in the energy-harvesting mode, by presenting the results obtained during an experimental campaign. This increased understanding can improve propeller designs, such that propellers can be used more efficiently in the energy-harvesting mode. This could lead to better propulsion integration benefits for distributed propeller concepts. Furthermore, validation data are scarce, especially for the energy-harvesting mode, and therefore more experimental data were also required. Moreover, as mentioned above, operating the propeller in energy-harvesting conditions will invert the aerodynamic loads on the blade sections and this inversion results in a reduction in axial velocity and the swirl will have an opposite sign. Therefore, the propeller-wing interaction will also be altered and the aerodynamic performance of the wing will be adversely affected. Insight into these slipstream phenomena will be important for future analyses of the performance of propeller-wing systems at negative thrust conditions.

II. Experimental Methods

A. Wind Tunnel Setup

A wind-tunnel experiment was performed to investigate the aerodynamic performance of a propeller that operates in both the propulsive and energy-harvesting regime. The experimental investigation was performed in the low-speed Low-Turbulence Tunnel (LTT) at Delft University of Technology. This low-speed wind tunnel is a closed-circuit wind tunnel and has an inflow turbulence level of around 0.03% for a free stream velocity of 40 m/s. The octagonal closed test section of 1.80 m x 1.25 m was used in which the propeller was placed in the center, while it was suspended from the ceiling, connected to the external balance. Fig. 2a displays a photograph of the test setup inside the test section as seen from the front.

A three-bladed version of the TUD-XPROP propeller was used and this propeller is representative of the propeller used on turboprop aircraft. Note that this propeller was not designed for energy-harvesting operations. The propeller has a diameter of 0.4064 m with a nacelle diameter of 0.0920 m. The blades, which do not contain any sweep, are manufactured from carbon fiber. The blade geometry is presented in Fig. 3, where the schematic blade layout is shown in Fig. 3a, and the chord and pitch distributions of the blades are presented in Fig. 3b. In the former, also different

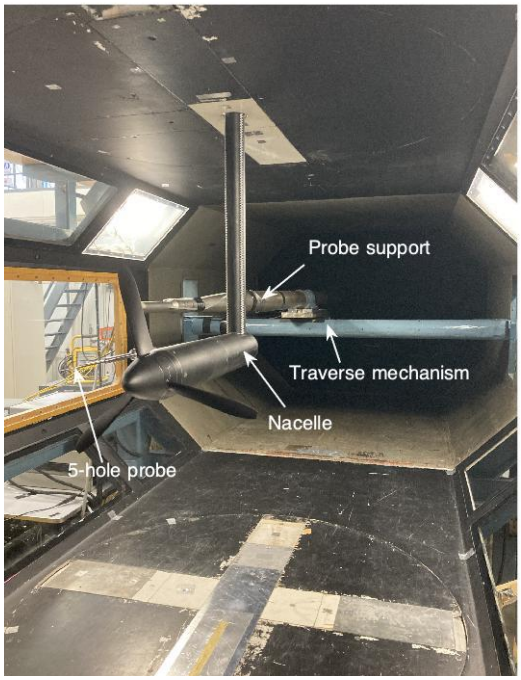

(a) Overview of the test setup including main components

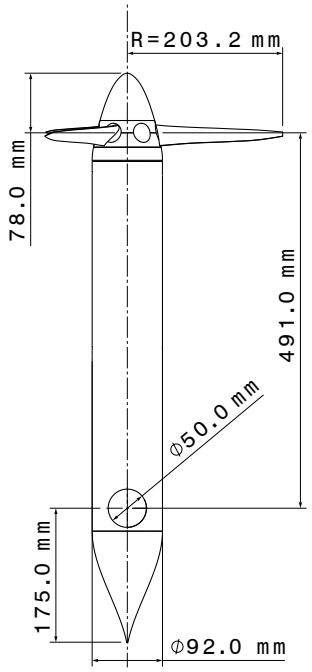

(b) Top view including relevant dimensions

Fig. 2 Propeller test setup

Downloaded by TU DELFT on August 16, 2022 | http://arc.aiaa.org | DOI: 10.2514/6.2022-3893

airfoil sections are shown, which are drawn up to scale with respect to the blade planform. Three blades were removed from the original six-bladed propeller to limit power requirements in propulsive and energy-harvesting regimes while keeping a representative blade loading condition. The round support sting was located at 491 mm ($1.2D_\mathrm{p}$) from the propeller plane, to reduce the upstream effect of the sting on the blade performance. Fig. 2b shows a schematic top view of the propeller setup, including relevant dimensions. Furthermore, zig-zag strips were placed on the support sting to trip the boundary layer to prevent laminar vortex shedding from the sting. Finally, an aerodynamically designed aft-cone was placed at the end of the nacelle to reduce the drag of the system. The propeller was operated with an electric motor, housed inside the nacelle, and the time-averaged rotational speed could be set with a precision of ±0.01 Hz. Fluctuations in rotational speed at a given set point were measured to be 0.1 Hz at most. The blade pitch angle could be set manually up to an accuracy of ±0.05°. For this experiment, the blade pitch angle was defined at 70% of the blade radius.

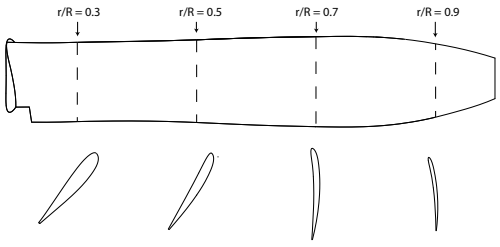

(a) Schematic blade layout with airfoil sections

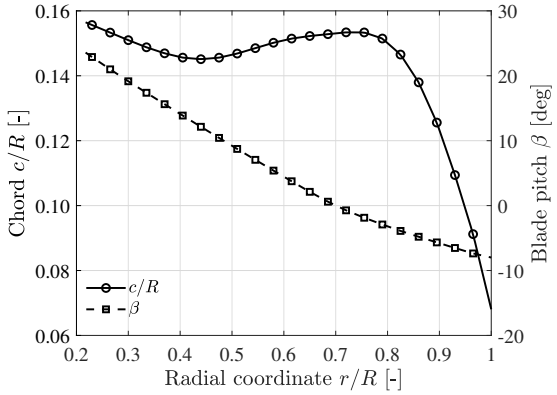

(b) Blade chord and pitch distributions

Fig. 3 TUD-XPROP propeller blade geometry for $\beta_{0.7R} = 0°$

B. Measurement Techniques

1. External Balance & Load Cell

The propeller sting was connected to the six-component external balance of the wind tunnel (not depicted in Fig. 2a). Therefore, all system forces and moments, including that of the support structure were measured by the external balance. The external balance has a high accuracy of around ±0.1 N and is hardly influenced by the operating conditions inside the test section, and therefore, there will be no temperature effect on the external balance readings. The external balance data were acquired at 10 Hz and averaged over 5 seconds of measurement time. The downside of using the external balance is the fact that the propeller performance cannot be completely isolated. Measurements with the blades removed were performed to estimate the propeller-off performance of the support structure. However, there will always remain an additional component in the propeller-on readings, due to the interaction of the slipstream with the support structure, which cannot be isolated.

To avoid this interaction component, an internal six-component load cell, mounted to the electric motor, was used to measure the isolated propeller performance. The load cell was calibrated for a full-scale load range of 480 N (±0.12 N), 240 N (±0.07 N), and 12 Nm (±0.001 Nm) for thrust, in-plane forces, and torque, respectively. In every measurement run, the measurement sequence was randomized to convert potential drifts within a measurement run into random errors. The load cell data were acquired at 10 kHz and also averaged over 5 seconds per measurement. Additionally, repeated measurements were performed spanning multiple days and after configuration changes to verify the reproducibility of the readings. Temperature variations inside the nacelle were caused by the electric motor and this impacted the strain gauge readings of the load cell. Since no temperature information of the load cell was available during the experiment, the temperature of the electric motor housing was used as an estimate of the load cell temperature. For a single measurement run, a linear fit between the starting and ending temperature was used to correct for the drift in output readings due to the change in temperature. Despite this correction method, the spread in thrust readings was found to be up to ±1 N, which is relatively large for the encountered measurement range, and hence much more than the initial uncertainty of the load cell. The data of the load cell were compared with the that of the external balance and it was concluded that the large spread was caused by the temperature sensitivity of the strain-gauge bridge that is dominated by the thrust component, in combination with the relatively small loading compared to the full-scale range for this component. This large spread was primarily found for high pitch settings, for which the motor was operating less efficiently and the temperature was more difficult to control. The differences between repeated measurement runs were found to be comparable to the scatter observed within a single run. The spread for the torque was found to be much smaller due to a lower temperature sensitivity of the strain-gauge bridge dominated by the torque. The spread in the thrust data from the load cell is further discussed in Sec. III.A.1 together with the comparison with the external balance data.

2. 5-Hole Pressure Probe

The obtain a better understanding of the observed integral performance, a 5-hole pressure probe was used to measure the total pressure inside the slipstream. The total pressure distribution measured close to the blades is representative of the loading distribution on the propeller blades. Furthermore, a pitot tube was placed in front of the model at the side of the test section to measure the total and static pressure in the free stream. The pressure measurements were performed using a DTC Initium pressure scanner system. The measurement uncertainty of this system was estimated to be ±4 Pa. The 5-hole probe was used since it has a higher accuracy than a standard pitot tube when there is a relatively large inflow angle (>5°), which is the case in the propeller slipstream due to the swirl component. The layout of the 5-hole probe is presented in Fig. 4, together with a closed-up cut-through of the tip, and the definition of the hole numbers [11]. The 5-hole probe has a center hole, numbered as hole 5, and 4 surrounding holes. In the experiment, the probe was mounted such that holes number 1 and 3 were aligned with the vertical (Z) axis, while holes 2 and 4 were aligned with the horizontal (Y) axis. For the 5-hole probe, the measurements were also averaged over 5 seconds. Measurements were taken in both the propulsive and energy-harvesting regime at three specific advance ratios. The precise experimental conditions for the slipstream analyses are discussed in Sec. II.C.

The measurements were performed in a plane of $1.0R$ x $1.0R$ behind the blades parallel to the rotation axis, which is schematically shown in Fig. 6a. Note that the edge of the analysis plane was located at 3.0 mm behind the propeller rotational plane. In the analysis plane, 10 different streamwise rows were analyzed, with each containing 25 points in the direction of the blade span, adding up to a total of 250 points. The measurement points were closer together near the tip region to increase the spatial resolution near the slipstream boundary, since the largest gradients were expected

Downloaded by TU DELFT on August 16, 2022 | http://arc.aiaa.org | DOI: 10.2514/6.2022-3893

Downloaded by TU DELFT on August 16, 2022 | http://arc.aiaa.org | DOI: 10.2514/6.2022-3893

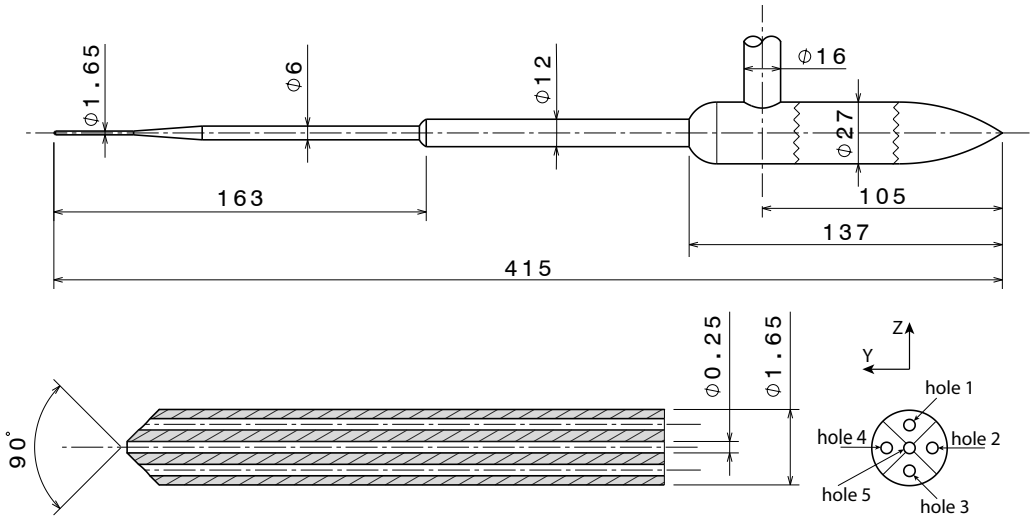

Fig. 4 Layout of the 5-hole probe (derived from [11]) including dimensions in mm

there. The lowest spatial resolution in the radial direction was around 10 mm, close to the root part of the blade, while it was around 1 mm near the tip region of the blade. The 10 streamwise rows were spaced equally in the analysis plane, leading to a spatial resolution of around 20 mm in the streamwise direction. The 5-hole pressure probe was also used to assess the azimuthal uniformity of the slipstream and hence to validate that the used horizontal analysis plane is representative for all circumferential positions. This was done by analyzing the total pressure in circumferential planes behind the blades, perpendicular to the rotation axis. These analysis planes are schematically shown in Fig. 6b. Due to the limitations in the physical access of the 5-hole probe around the model, not a complete half of the slipstream could be analyzed. Before the 5-hole probe measurements were done, a calibration procedure was performed in the LTT to correlate the measured pressures to the inflow conditions of the probe. Non-dimensionalized pressure coefficients are being used to determine the velocity field characteristics and they are defined by using the following equations:

$$C_{p_{13}} = \frac{p_1 - p_3}{p_5 - p_{av}} \quad (1) \qquad C_{p_{24}} = \frac{p_2 - p_4}{p_5 - p_{av}} \quad (2) \qquad C_{p_t} = \frac{p_5 - p_t}{p_5 - p_{av}} \quad (3) \qquad C_{p_s} = \frac{p_{av} - p_s}{p_5 - p_{av}} \quad (4) \qquad p_{av} = \frac{\sum_{n=1}^{4} p_n}{4} \quad (5)$$

with p_n the pressure from hole n, and p_t and p_s the local total and static pressure at the probe location respectively. The results from the calibration in terms of $C_{p_{13}}$, $C_{p_{24}}$ and C_{p_t} as function of the angle of attack and sideslip are shown in Fig 5a, 5b and 5c respectively. So from the calibration, the response models for C_{p_t} and C_{p_s} as function of $C_{p_{13}}$ and $C_{p_{24}}$ can be constructed. Using these, the local p_t and p_s at the probe location can be determined for a specific inflow field during the experiment.

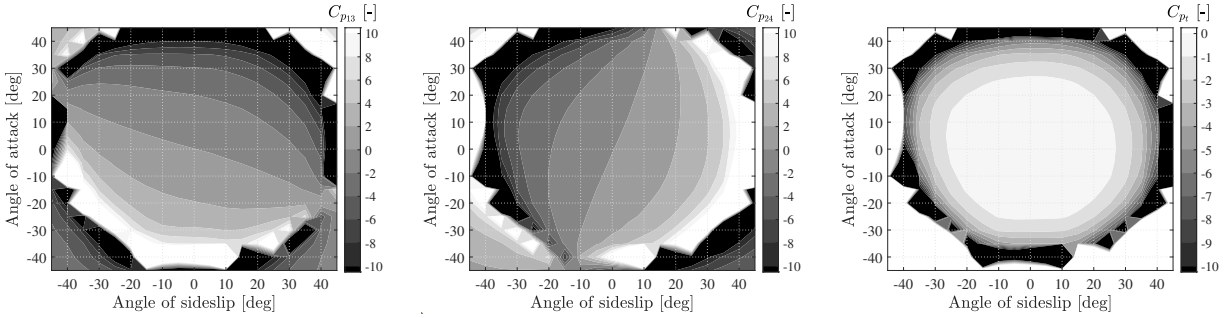

(a) $C_{p_{13}}$ **(b)** $C_{p_{24}}$ **(c)** C_{p_t}

Fig. 5 Relevant pressure coefficients as function of angle of attack and angle of sideslip from the 5-hole probe calibration

It turned out that the uncertainty in the total pressure was large for angles higher than 30°, and thus restricting the usability of the probe in terms of inflow angle. This can also be seen in the calibration contours, which show patchy behavior for angles larger than this. This is due to the denominator in the pressure coefficient equations going to zero, and for even larger angles, it becomes negative, due to the separation at the probe tip. Alternative calibration procedures are possible, but were not considered for the work described in this paper. The response model of C_{p_s} was similar to that of C_{p_t}. The response models were fitted for the data within the ± 30° range in terms of angle of attack and angle of sideslip. For the advance ratios examined in the experiment, the swirl angle in the slipstream turned out to be lower than 10°. for the swirl angles encountered in the experiment, the calibration procedure yielded an uncertainty of about 0.5% in the local total pressure.

3. Particle Image Velocimetry

To further investigate the aerodynamics of the propeller in energy-harvesting mode, the slipstream velocity field was analyzed. The velocity distributions in the slipstream can yield relevant information for the installed propeller-wing configuration. Stereoscopic PIV was performed in a plane behind the blades parallel to the rotation axis, similar to the 5-hole probe measurements. Both phase-locked and phase-averaged PIV measurements were performed for the same advance ratios as for the 5-hole probe measurements, such that the results could be correlated. The capability to get time-dependent information is a key benefit compared to the 5-hole probe measurements. The total field of view included the propeller blades and the nacelle, leading to an effective evaluation plane that was approximately equivalent to the 5-hole probe analysis plane, see Fig. 6a. The phase-locked measurements were triggered by the one-per-revolution signal from the optical encoder installed on the motor shaft to synchronize the image acquisition with the propeller rotational speed. During these phase-locked PIV measurements, the phase angle of the propeller was set to zero with respect to the analysis plane, meaning one of the blades was centered around the laser sheet.

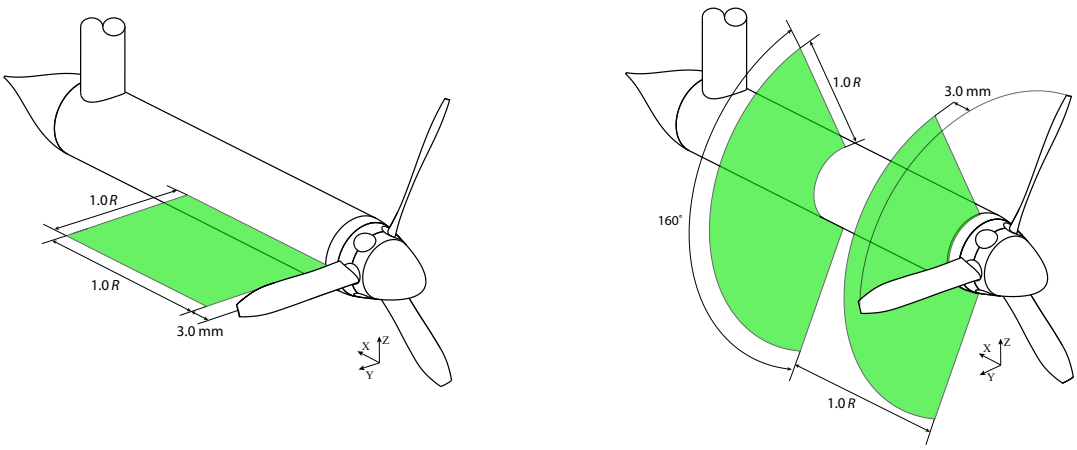

(a) Horizontal plane used for both PIV and 5-hole probe measurements

(b) Circumferential planes used for the 5-hole probe measurements to assess the slipstream uniformity

Fig. 6 Position of the evaluation planes for the slipstream analysis

The tracer particles, created by a mixture of diethylene-glycol and water, were inserted into the tunnel. The 200 mJ Nd:YAG laser and two sCMOS cameras (16-bit 2560 px x 2160 px) were placed outside the test section, on a traversing system, such that the whole setup could move up- or downstream. This was done such that the evaluation plane was analyzed in two steps, to increase the spatial resolution. The two cameras, equipped with 105 mm lenses, were placed on a vertical fixture, hence the cameras were looking from the top and bottom to the laser sheet, while having the same streamwise position. For the phase-averaged measurements, 2000 uncorrelated image pairs were acquired, while for the phase-locked measurements, 500 image pairs were acquired. The main characteristics of the PIV setup are presented in Table 1. Only a single calibration was performed, namely in the first frame, which contained the propeller blades. For the second field-of-view, which was located more downstream, it was assumed that the same calibration would suffice. However, it turned out that the second image plane was slightly rotated with respect to the first, leading to an additional out-of-plane uncertainty.

Downloaded by TU DELFT on August 16, 2022 | http://arc.aiaa.org | DOI: 10.2514/6.2022-3893

Table 1 Characteristics of the PIV setup

Parameter	Value	Parameter	Value
PIV setup	Stereoscopic	Image pair separation time (Δt)	20 μs
Laser type	Nd:YAG	Image pairs	500, 2000
Camera type	sCMOS	Interrogation window size	32 x 32 pixels
Objective	105 mm $f/5.6$	Overlap factor	50%
Field of view	1.25 R x 1.25 R	Spatial resolution	0.50 mm
Digital resolution	17 px/mm	Maximum velocity uncertainty	1.5%

C. Test Conditions

The propeller performance was determined at a constant free stream velocity, with 5 different blade pitch settings, ranging from 10° to 30° in steps of 5°. The used electric motor was limited in terms of torque, and hence a free stream velocity of 30 m/s was used, such that also reasonable positive trust settings could be achieved for the different pitch settings. Higher pitch settings could not be achieved due to these limitations. The propeller was operated in both propulsive and energy-harvesting conditions and depending on the specific pitch setting, a different range of advance ratios was tested. The overview of the considered conditions can be seen in Table 2. The lower bound on the advance ratio was mainly determined by the available power of the electric motor, while the upper bound was chosen rather arbitrarily, but it was ensured that a large portion of the energy-harvesting regime was tested, including the point of maximum energy output. All measurements were performed in symmetric inflow conditions, meaning 0° angle of attack and sideslip for the propeller-nacelle model.

Table 2 Advance ratio sweeps for different pitch angles at V_∞ = 30 m/s

$\beta_{0.7R} = 10°$	$\beta_{0.7R} = 15°$	$\beta_{0.7R} = 20°$	$\beta_{0.7R} = 25°$	$\beta_{0.7R} = 30°$
$0.50 < J < 1.50$	$0.55 < J < 1.50$	$0.65 < J < 1.90$	$0.80 < J < 2.00$	$0.90 < J < 2.10$

For $\beta_{0.7R}$ = 15° and 30°, also runs at different free stream velocities were performed, to estimate the effects of two key similarity parameters on the propeller performance, namely the Reynolds and Mach number. The former was chosen since it was found in previous numerical work that it was close to the optimal pitch for maximum energy-harvesting performance [8], although for a different propeller. The latter pitch setting was chosen to have a more realistic pitch setting compared to actual flight with positive thrust. For these two pitch settings, the wind tunnel velocity was varied from 20 to 40 m/s. In this way, the same advance ratios could be analyzed at different Reynolds and Mach numbers. The total overview of analyzed operational conditions can be seen in Table 3. The upper and lower bounds in advance ratio were slightly shifted for different free stream velocities due to the limitations of the electric motor. The Reynolds numbers mentioned are calculated using the local effective velocity and blade chord at 70% of the blade radius, while the Mach number was calculated for the tip section. The effective velocity is the vector summation of the free stream velocity and the circumferential velocity, see Fig. 1. Note that for both similarity parameters, the local effective velocity was calculated without taking the induced velocities into account.

Table 3 Advance ratio sweeps for different free stream velocities including Reynolds and tip Mach number ranges

	V_∞ = 20 m/s	V_∞ = 30 m/s	V_∞ = 40 m/s
$\beta_{0.7R} = 15°$	$1.50 > J > 0.55$ $0.72 < Re_{0.7R} \cdot 10^5 < 1.83$ $0.13 < M_{\text{tip}} < 0.34$	$1.50 > J > 0.55$ $1.07 < Re_{0.7R} \cdot 10^5 < 2.74$ $0.20 < M_{\text{tip}} < 0.51$	$1.50 > J > 0.65$ $1.42 < Re_{0.7R} \cdot 10^5 < 2.91$ $0.27 < M_{\text{tip}} < 0.57$
$\beta_{0.7R} = 30°$	$1.90 > J > 0.70$ $0.64 < Re_{0.7R} \cdot 10^5 < 1.45$ $0.11 < M_{\text{tip}} < 0.27$	$2.10 > J > 0.90$ $0.87 < Re_{0.7R} \cdot 10^5 < 1.75$ $0.16 < M_{\text{tip}} < 0.32$	$2.20 > J > 1.10$ $1.13 < Re_{0.7R} \cdot 10^5 < 1.96$ $0.20 < M_{\text{tip}} < 0.36$

Downloaded by TU DELFT on August 16, 2022 | http://arc.aiaa.org | DOI: 10.2514/6.2022-3893

Finally, the slipstream flow field was analyzed for three specific advance ratios and the data were obtained using PIV and the 5-hole probe as discussed before. These advance ratios were the point of maximum propeller efficiency, the point of zero thrust, and the point of maximum energy-harvesting efficiency. The corresponding advance ratios were estimated based on a blade-element-momentum analysis. The slipstream analysis was done at a fixed free stream velocity of 30 m/s and for the same two pitch settings as for the similarity parameter analysis. An overview of the analyzed advance ratios can be seen in Table 4.

Table 4 Specific advance ratios for the slipstream analysis at V_∞ = 30 m/s

	Propulsive	Zero thrust	Energy harvesting
$\beta_{0.7R} = 15°$	$J = 0.60$	$J = 0.75$	$J = 1.10$
$\beta_{0.7R} = 30°$	$J = 1.20$	$J = 1.40$	$J = 1.90$

Downloaded by TU DELFT on August 16, 2022 | http://arc.aiaa.org | DOI: 10.2514/6.2022-3893

III. Results

The results from the wind tunnel test are presented in this section. Starting in Sec. III.A, the aerodynamic propeller performance is presented. Subsequently, the total pressure distributions in the slipstream is presented in Sec. III.B. The observed blade sectional performance will determine the slipstream velocity distributions. The slipstream velocity distributions are shown in Sec. III.C.

A. Integral Aerodynamic Performance

Propeller performance can be presented using different non-dimensionalized coefficients. For the propeller performance on aircraft design level, the thrust and power are normalized using the free stream velocity and the disk area, leading tot T_C and P_C. However, for the discussion of the performance at the blade level, the most suitable performance indicators are the thrust and power coefficient C_T and C_P, which are based on normalization with an effective dynamic pressure defined with respect to the rotational velocity of the propeller.

1. Thrust Data Spread

During the experiment, a large scatter was found between repeated runs for the thrust coefficient, as was discussed in Sec. II.B. This was due to the temperature sensitivity of the thrust output from the load cell. Especially at low absolute thrust, the error due to the temperature sensitivity becomes significant, because the load is small compared to the full range of the load cell. By randomizing the order of the measurement points within runs and by sufficient repetition, the impact of the resulting measurement error on the overall performance trend was minimized. To confirm that the large spread was caused by temperature effects rather than random errors, the load cell thrust readings were compared with the external balance data in terms of thrust coefficient (C_T). Since the output readings from external balance are not influenced by changes in temperature, the spread in C_T is expected to be much smaller than that of the load cell.

In Fig. 7, the raw C_T-data are shown for $\beta_{0.7R} = 15°$ and 30°, indicated by the markers. Each data set contained more than 200 data points, obtained during different runs. To describe the performance of the propeller in the considered J-range, 4th-order polynomial fits were used for the thrust and power coefficients. 95% confidence intervals were added to the fitted curves, but are indistinguishable from the fitted curves due to the large number of measurements performed, reducing the width of the intervals. In Fig. 7a the load cell data are shown while in Fig. 7b the thrust readings from the external balance are shown. The latter is defined as the net thrust of the balance by $T = T_{\text{prop-on}} - T_{\text{prop-off}}$. Note that the calculated thrust from the external balance will be different than the thrust from the load cell due to the slipstream-interaction component which can not be isolated. The spread in C_T load cell data for the $\beta_{0.7R} = 15°$ case is much smaller than for $\beta_{0.7R} = 30°$, since the temperature could be controlled much better for the former, due to the lower shaft torque for this blade pitch. The external balance shows less spread than the load cell, which is primarily visible for the $\beta_{0.7R} = 30°$ case, confirming that the large spread is caused by the uncertainty in temperature calibration. The trends for the load cell data are similar to that of the external balance, confirming that the two ways of measuring the propeller thrust are equivalent. However, the external balance data thrust curves seem to slightly under-predict the thrust in both propulsive and energy-harvesting conditions compared to the load cell. The maximum difference is around 5% in terms of C_T over the advance ratio ranges considered for both pitch settings, which is caused by the slipstream interaction component that is included in the external balance data. In the propulsive mode, the increased axial velocity

in the slipstream will increase the friction drag on the support structure compared to the prop-off measurements, leading to a lower net positive thrust. In the energy-harvesting mode, there will be a decreased axial velocity in the slipstream, reducing the friction drag. However, since the thrust of the propeller is also negative, the correction from the prop-off measurements will again lead to an under-prediction in thrust. So the external balance fitted curve has a slightly smaller slope.

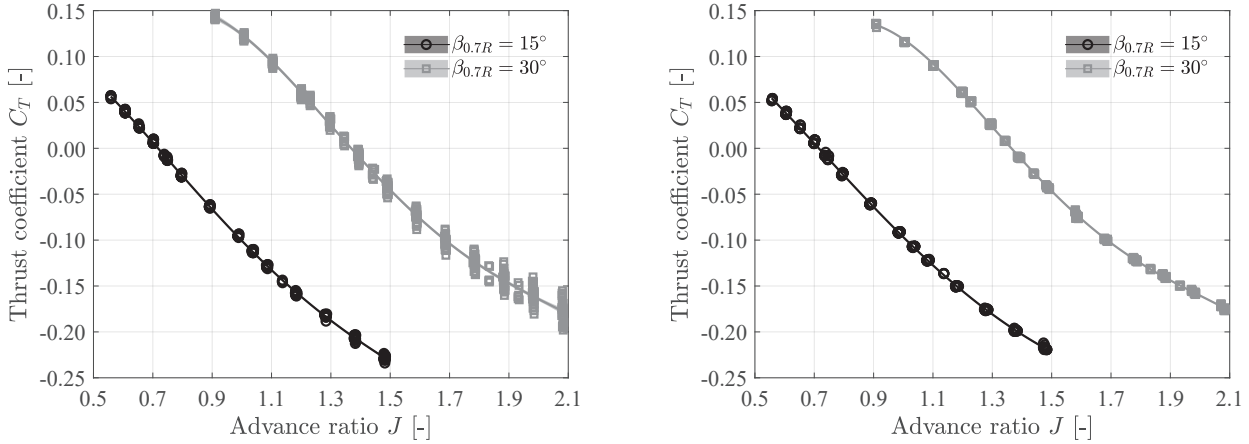

(a) Load cell data **(b) External balance data**

Fig. 7 Comparison between load cell and external balance thrust coefficient versus advance ratio for two different pitch settings

2. Propeller Thrust and Power

In Fig. 8, the aerodynamic performance of the propeller is shown for all considered pitch settings in terms of the thrust coefficient (C_T) and the power coefficient (C_P) in Fig. 8a and Fig. 8b respectively. Note that the torque and power are simply connected by the rotational speed ($P = 2\pi n \cdot Q$). The 4th-order polynomial fits are shown together with the 95% confidence interval, while the raw data points were left out for clarity. For the lower pitch settings, the thrust coefficient in the propulsive mode is almost linear with advance ratio, as is expected at these low loading conditions [5]. The change in pitch setting shifts the $C_T - J$ curve horizontally. For the higher pitch setting, the same thrust coefficient is reached at a higher advance ratio compared to the lower pitch setting. That means that for a given C_T, the absolute thrust is lower at the high pitch setting than at the lower pitch setting. When the pitch setting is increased, the non-linear part of the $C_T - J$ curve starts to be visible. Since the induction is relatively low for the higher pitch settings, this non-linearity is primarily caused by the large positive angles of attack on the blade sections, indicating blade separation in the propulsive regime. The C_P curves show a linear behavior in low-thrust conditions, similar to the thrust coefficient. For the high-thrust settings, the power coefficient flattens, meaning the required absolute power increases rapidly with a small decrease in advance ratio. This is again due to separation on the blades caused by the high positive angles of attack.

The thrust and power coefficient keep on decreasing with further increase in advance ratio because the inflow angle increases, which leads to a lower angle of attack for a given pitch setting, see Fig. 1. Since these measurements were performed at constant free stream velocity, the advance ratio was increased by decreasing the rotational speed. If the flow angle becomes larger than the local pitch angle, it will lead to negative angles of attack on the blade sections. For the lowest pitch setting of $\beta_{0.7R} = 10°$, almost the whole rotational speed range leads to negative thrust output of the propeller, caused by negative angles of attack on the blade, as shown in Fig. 1b. For each pitch setting, the propeller enters the braking mode at a specific advance ratio, for which it starts to create negative thrust, while still requiring positive power. The braking mode spans a larger advance ratio domain for the lower pitch settings. This is due to the fact that for the low pitch settings, the negative lift vector (C_l) obtained at small negative angles of attack is directed primarily in the direction of the thrust vector (C_t), as can be seen in Fig. 9a. In this situation, the component of the drag in the direction of the positive torque will be larger than that of the negative lift, pointing in the opposite direction, and hence a positive power is still required. When the advance ratio is increased and the angle of attack is increased, the

Downloaded by TU DELFT on August 16, 2022 | http://arc.aiaa.org | DOI: 10.2514/6.2022-3893

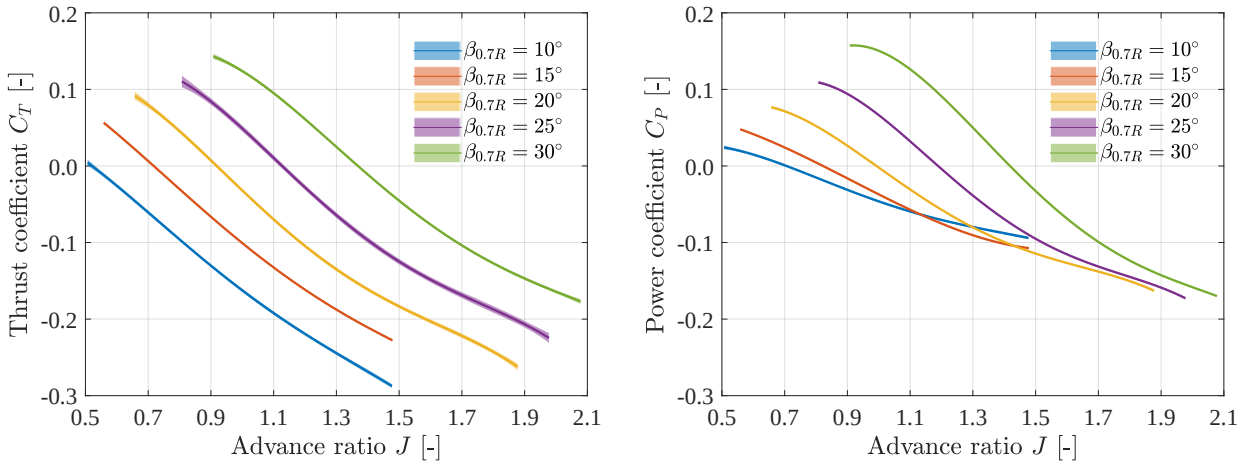

(a) Thrust coefficient versus advance ratio

(b) Power coefficient versus advance ratio

Fig. 8 Propeller performance at V_∞ = 30 m/s for the different pitch settings

Downloaded by TU DELFT on August 16, 2022 | http://arc.aiaa.org | DOI: 10.2514/6.2022-3893

negative lift vector will start to contribute more towards the negative torque, overcoming the opposing drag component. There is a relatively large change in inflow angle needed to enter the energy-harvesting mode. However, for the higher pitch setting, the negative lift vector obtained at small negative angles of attack will already point largely in the direction of the negative torque, as can be seen in Fig. 9b. So for low pitch settings, it takes a larger negative angle of attack to end up in the energy-harvesting mode compared to high pitch settings, meaning the braking mode spans a larger advance ratio range for the former.

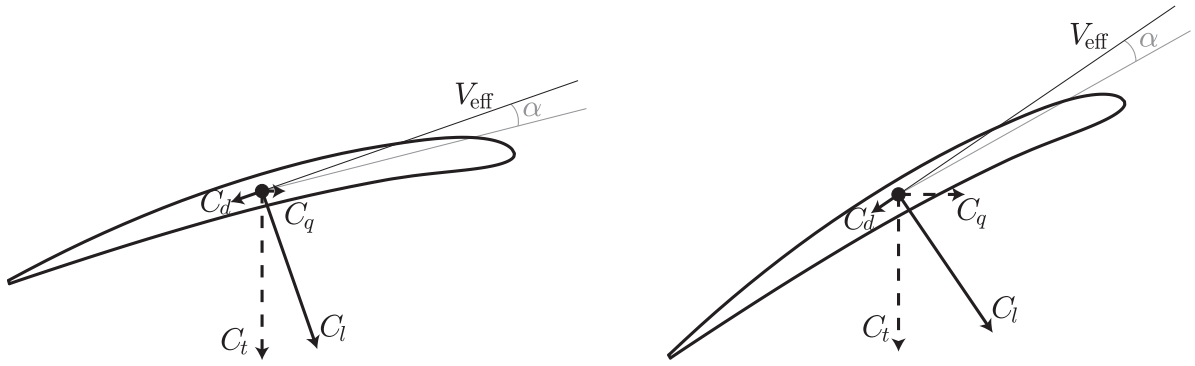

(a) Low pitch setting

(b) High pitch setting

Fig. 9 Relevant blade forces during energy-harvesting for different pitch settings assuming equal aerodynamic performance

In the energy-harvesting mode, the C_T keeps on decreasing, also in a linear fashion for the first part. Finally, for higher advance ratios, the absolute thrust and power of the propeller in the energy-harvesting regime flatten or even reduce in magnitude due to the increasingly more negative angle of attack on the blade sections, which leads to stall on the blade sections, reducing the negative lift and hence the negative thrust. The kinks in the C_T curves in the energy-harvesting regime mark the end of the linear flow regime, meaning the blade sections are close to stall. From this point onward, the negative thrust will increase marginally with increasing advance ratio until reaching the maximum negative thrust condition, after which the negative thrust will flatten or even reduce. For a fixed advance ratio, a lower pitch setting leads to a higher negative thrust, since the negative angles of attack will be simply larger than for a higher

pitch setting. To more clearly analyze the decrease in thrust in the energy-harvesting regime, the T_C is plotted for different pitch settings in Fig. 10a and note that $T_C = C_T J^{-2}$. When the values of T_C are examined, it can be seen that the absolute thrust values are decreasing again after the point of maximum negative thrust for the low pitch settings, while those of high pitch settings remain more flat. This can be explained again by looking at Fig. 9. For the low pitch setting, any decrease in negative lift due to stall will quickly decrease the negative thrust, while the associated increase in drag does not contribute much to the negative thrust. However, for high pitch settings, the same decrease in lift will be more compensated for by the increase in drag, due to the higher flow angle at which this stall is reached. This compensating effect becomes larger for higher advance ratios and hence explains the eventual flattening of the curves. For a fixed negative angle of attack, hence for a given C_l and C_d on the blade sections, the low pitch setting will have a higher negative C_t and a lower C_q compared to a higher pitch setting.

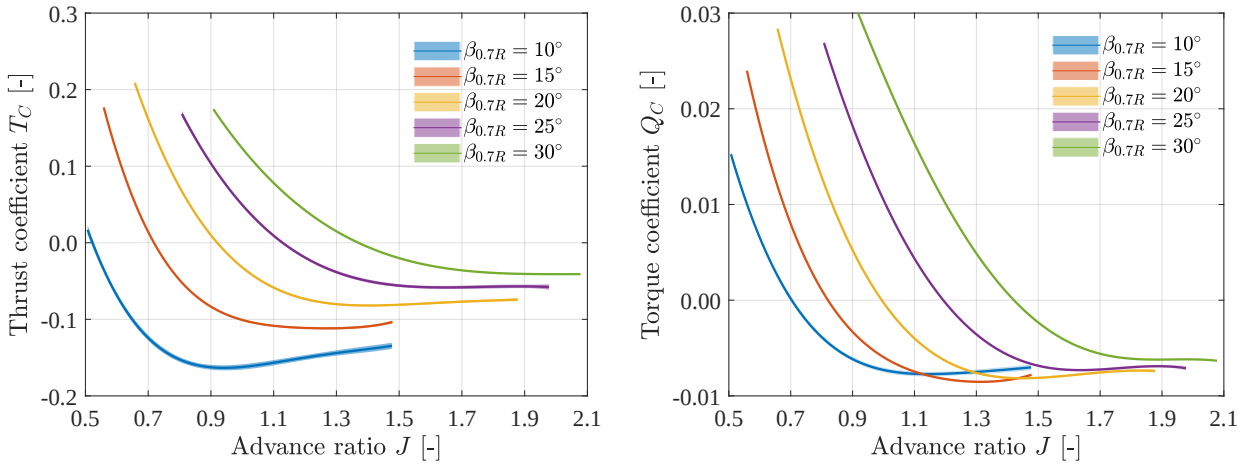

(a) Thrust coefficient versus advance ratio

(b) Torque coefficient versus advance ratio

Fig. 10 Propeller performance at V_∞ = 30 m/s for the different pitch settings

For the C_P (Fig. 8b), the trends in the energy-harvesting mode are different than for C_T, and the curves flatten earlier than the thrust coefficient due to the fact that the increase in negative lift and increase in drag oppose each other for the negative power on the blade sections, which is especially visible for the pitch setting of $\beta_{0.7R} = 10°$. Similar to the thrust curves, the low pitch setting shows even a reduction in absolute power, which is visible by the low slope, while the higher pitch settings seem to have a more flat absolute power distribution. The increase in the negative angle of attack will be offset by a decrease in local dynamic pressure in terms of absolute forces. It seems that the negative power converges to a value independent of the pitch setting, since all the curves start to overlap. From the C_P curves, it is difficult to assess the absolute power that is being generated by the propeller and which pitch setting is more beneficial in terms of energy harvesting. Therefore, the energy-harvesting efficiency is a better indicator of the harvested power. This value will be discussed in Sec. III.A.4.

3. Scaling Effects

The wind tunnel operates at atmospheric conditions and the relatively low free stream velocity used leads to a low Reynolds and Mach number. The full-size propeller will experience a much higher Reynolds and tip Mach number than the scaled propeller used in this experiment. To investigate the impact of the Reynolds and Mach number on the performance of the blades, runs were performed at different free stream velocities. This was done for the pitch setting of $\beta_{0.7R} = 15°$ and $\beta_{0.7R} = 30°$. A lower Reynolds number results in a thicker boundary layer on the blade sections and hence a more non-linear lift curve slope. A thicker boundary layer on the blade sections will also lower the maximum absolute lift, both for positive and negative angles of attack. Furthermore, possible laminar separation could lead to sudden performance degradation. An increase in Reynolds number will increase the propeller performance, together with its efficiency. The decrease in tip Mach number yields a decrease in aerodynamic performance due to the lack of compressibility. An increase in Mach number will, similarly to the Reynolds number, increase the slope of the thrust and power curves. In Fig. 11, the C_T and C_P data are shown for $\beta_{0.7R} = 15°$. The values of the Reynolds and tip Mach

Downloaded by TU DELFT on August 16, 2022 | http://arc.aiaa.org | DOI: 10.2514/6.2022-3893

number encountered were discussed in Sec. II.C. The variation in the similarity parameters for a fixed free stream velocity is actually caused by the change in rotational speed. So for a fixed advance ratio, the change in free stream velocities is accompanied by a change in rational speed leading to an increase in Reynolds and Mach number. It is known that for Reynolds numbers below $1.5{\cdot}10^5$, defined using the local chord and effective velocity at 70% of the blade span, the performance of this propeller becomes very sensitive to the inflow conditions [12].

There is an increase in both thrust and power coefficients, when the Reynolds number and tip Mach number are increased, which is caused by an increase in the lift coefficient on the blade sections. There will also be a decrease in C_P due to the decrease in C_d, but this will be offset by the increase in C_P due to C_l. However, the increase in C_T is more than the increase in C_P, hence the efficiency of the propeller is also increased. The increase in C_l and decrease in C_d will cause a shift in the advance ratio at which the propeller enters the braking mode. The increased slope of the lift curve for the higher Reynolds and Mach number is also visible, since the $C_T - J$ curve is steeper for V_∞=40 m/s. The compressibility effects scale non-linearly with M, with increasing impact at higher M, which means that the J sweep at higher M_∞ will have a higher rate of change of compressibility effects. In the energy-harvesting mode, similar conclusions can be drawn, where the negative thrust is increased with increasing Reynolds number. However, the differences seem to become much smaller, which could either indicate that the flow phenomena at these advance ratios are not being driven by a (small) change in Reynolds number, or that the Mach number effect is dominant over the Reynolds number effect but its impact is smaller in the energy-harvesting mode because the absolute values of the tip Mach number are lower. The large variation for V_∞=20 m/s compared with the other curves in the energy-harvesting mode is caused by the spread obtained in the load cell readings, since this large discrepancy was not present in the external balance data. This larger spread was due to the lower absolute thrust values at the low free stream velocity.

Downloaded by TU DELFT on August 16, 2022 | http://arc.aiaa.org | DOI: 10.2514/6.2022-3893

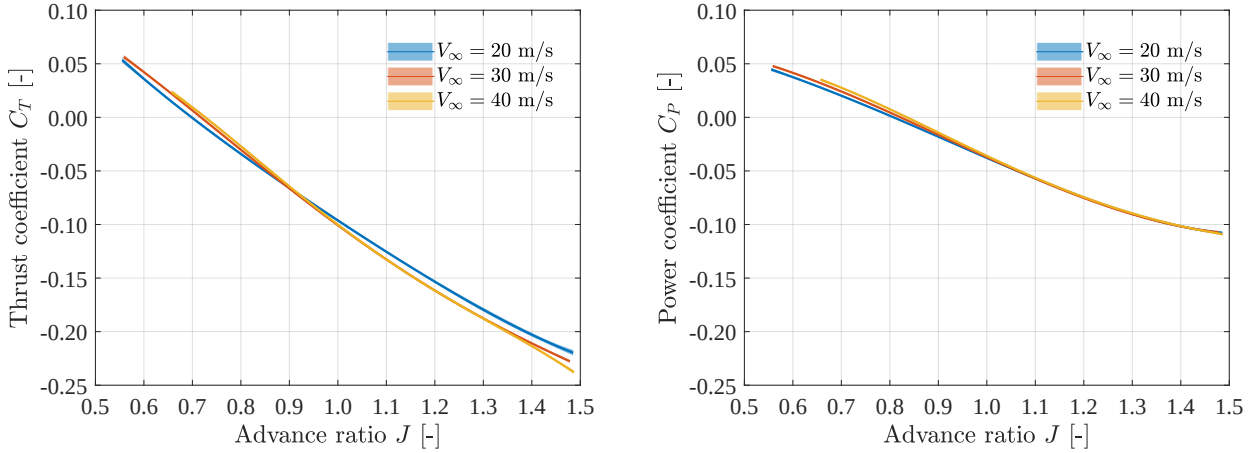

(a) Thrust coefficient versus advance ratio

(b) Power coefficient versus advance ratio

Fig. 11 Propeller performance at $\beta_{0.7R}$=15° for V_∞=20, 30 and 40 m/s

The differences in terms of C_P, between the runs with a different free stream velocity, in the energy-harvesting mode also seem to go to zero, similar to the observed differences in the thrust coefficient. Note that the differences between the free stream velocities for both thrust and power coefficient for $\beta_{0.7R} = 15°$ are rather small due to the fact that the propeller is operating at relatively high rotational speeds and hence a change in free stream velocity only contributes marginally to the total change in Reynolds and Mach number. The lower the rotational speed, the more influence the change in free stream velocity will have on the change in Reynolds and Mach number. In Fig. 12, the C_T and C_P data are shown for $\beta_{0.7R} = 30°$. Similar conclusions can be drawn as for the case of $\beta_{0.7R} = 15°$. The relative importance of the free stream velocity on the Reynolds and tip Mach number is more apparent, since the differences between the three curves are bigger compared to the low pitch setting. Furthermore, for a large part of the considered operational conditions, the Reynolds number was lower than the aforementioned $1.5 \cdot 10^5$ [8]. Note that the overall variation in Reynolds and tip Mach number at a fixed advance ratio was rather small compared to the absolute values of the two similarity parameters. Furthermore, the values were still far from realistic Reynolds and tip Mach numbers encountered in real flight conditions, hence conclusions regarding the energy-harvesting performance as function of the Reynolds and Mach number should be interpreted with caution.

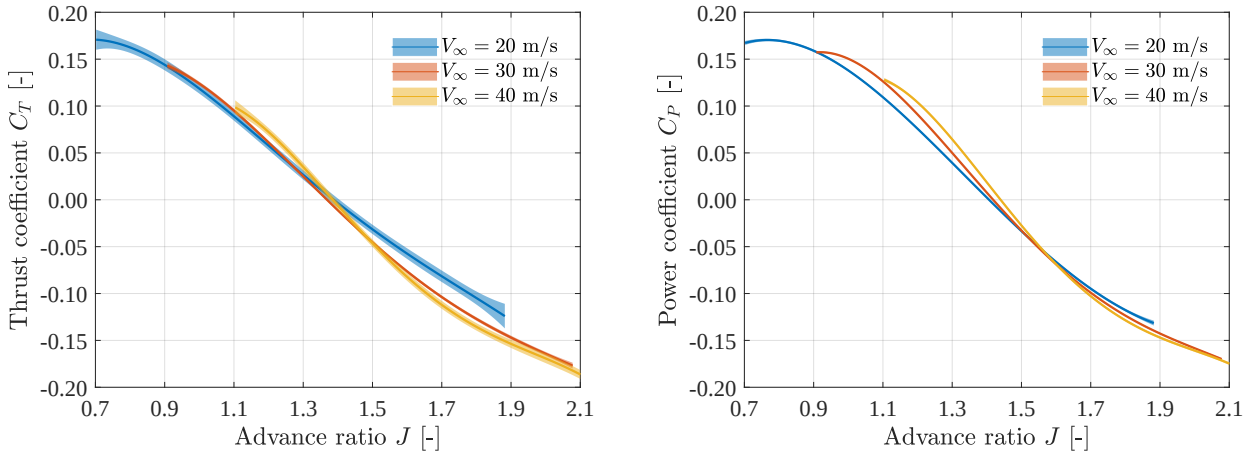

(a) Thrust coefficient versus advance ratio

(b) Power coefficient versus advance ratio

Fig. 12 Aerodynamic performance at $\beta_{0.7R}$=30° for V_∞=20, 30 and 40 m/s

4. Efficiency

To minimize fuel consumption in the propulsive regime, the propeller efficiency should be maximized. In the propulsive regime, the efficiency of the propeller is defined as the ratio of thrust power over the shaft power ($\eta_p = TV_\infty/P$). The propeller efficiency for the propeller at different pitch settings is shown in Fig. 13a. The efficiency is shown including the combined confidence interval of the 4th-order polynomial fits of the propeller thrust and power. As is expected, the propeller efficiency is larger for a higher pitch setting, since this condition is achieved at a lower thrust setting, which means lower axial induction losses. However, in the energy-harvesting regime, the propeller efficiency does not have any physical interpretation. In the energy-harvesting mode, it is more relevant to analyze the amount of power that is being extracted from the free stream. Therefore, the energy-harvesting efficiency (η_{eh}) is defined as the amount of power extracted from the total available power of the incoming flow that passes through the propeller disk (A). The energy-harvesting efficiency is linked to the power coefficient (P_C) according to Eq. 6. This definition is analogous to the definition of the efficiency used in wind turbine design, where the upper limit is defined by the Betz limit of 59%.

$$\eta_{eh} = \frac{-P}{\frac{1}{2}\rho V_\infty^3 A} = -\frac{8}{\pi} P_C \tag{6}$$

$$\eta_t = \frac{-P}{-TV_\infty} = \frac{1}{\eta_p} \tag{7}$$

In Fig. 13b, the energy-harvesting efficiency of the propeller is shown for the pitch settings from $\beta_{0.7R} = 10°$ up to 30°. The higher the pitch setting, the lower the advance ratio at which the maximum energy-harvesting efficiency is reached. From the data, it is confirmed that the energy-harvesting efficiency is rather low compared to equivalent wind turbines, similar to previous studies [8]. The low energy-harvesting is due to the blade design of this propeller, which is optimized for the propulsive mode. The highly cambered blade sections see large negative angles of attack in the energy-harvesting regime, which causes flow separation. This will be further analyzed when the total pressure distribution behind the blades is discussed, see Sec. III.B. A lower pitch setting allows for more energy harvesting, and it seems that the maximum is located in between $\beta_{0.7R} = 10°$ and 15° for this propeller.

When comparing two blade sections with the same aerodynamic performance but with different pitch settings, the low pitch setting would actually lead to a smaller negative C_q compared to the high pitch setting, as is shown in Fig. 9. However, for a fixed inflow power, hence a fixed free stream velocity, the condition of maximum energy harvesting is reached for the low pitch setting at a lower advance ratio and hence the local dynamic pressure is higher. It turns out that the absolute negative torque, therefore, does not vary much depending on the pitch setting at the maximum energy-harvesting condition. This is shown in Fig. 10b, where it can be seen that for the three lowest pitch settings, the maximum negative torque is similar. Therefore, assuming a fixed free stream velocity, a lower pitch setting tends towards a high energy-harvesting output power, due to the higher rotational speed at which the maximum energy-harvesting condition of the blade sections is reached. Unfortunately, as shown in Fig. 8a and Fig. 10a, this also comes at the cost of having more negative thrust.

Downloaded by TU DELFT on August 16, 2022 | http://arc.aiaa.org | DOI: 10.2514/6.2022-3893

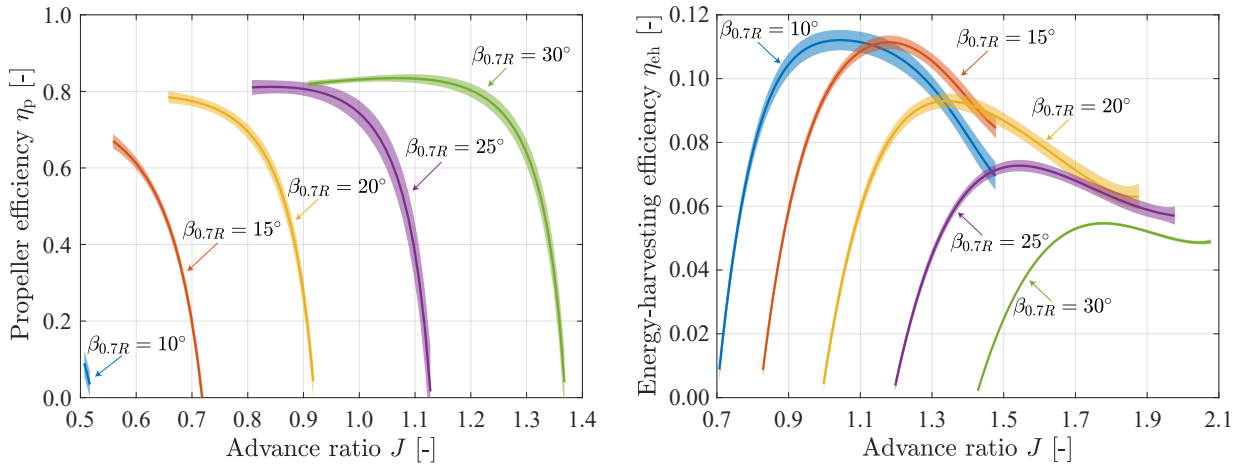

(a) Propeller efficiency versus advance ratio **(b) Energy-harvesting efficiency versus advance ratio**

Fig. 13 Propulsive and energy-harvesting efficiency at V_∞ = 30 m/s for the different pitch settings

For the energy-harvesting mode, the highest efficiency is achieved at a low pitch setting, while the propeller efficiency is highest for the higher pitch setting, meaning that a variable-pitch propeller should be used to maximize both efficiencies at the same time in real flight. However, as mentioned before, the negative power at low pitch settings is obtained due to the high rotational speed in combination with a large negative lift vector, even though this vector is pointing primarily in the direction of the negative trust. Decreasing the advance ratio and hence increasing the negative angles of attack could yield a more negative lift vector on the blade sections. However, for a fixed free stream velocity, this condition is then also reached at a lower rotational speed and this means a lower effective dynamic pressure, and hence smaller absolute forces. Furthermore, the increase in drag associated with the increased negative angles of attack will offset the increase in negative lift in terms of the negative power. When considering the use of energy-harvesting propellers on aircraft, the associated negative thrust (drag) is something that should be taken into account. Therefore, it would be also useful to analyze how efficiently the propeller can convert the negative lift and drag into negative power. To take this into account, a third efficiency is defined, called the turbine efficiency (η_t) in this paper. The definition is shown in Eq. 7 and it is the inverse of the propeller efficiency. So this efficiency is a measure of the propeller's ability to extract power from the free stream, as fraction of the drag power needed to reach this condition. The data of the η_t as function of the advance ratio for different pitch settings are shown in Fig. 14a.

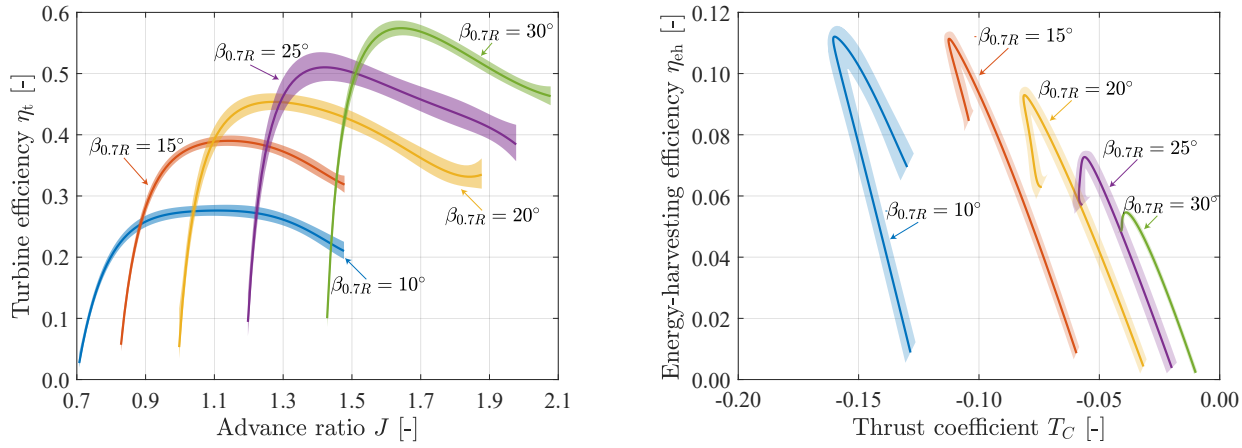

(a) Turbine efficiency versus advance ratio **(b) Energy-harvesting efficiency versus thrust coefficient**

Fig. 14 Efficiency in energy-harvesting conditions at V_∞ = 30 m/s for the different pitch settings

Downloaded by TU DELFT on August 16, 2022 | http://arc.aiaa.org | DOI: 10.2514/6.2022-3893

The trends of the observed turbine efficiency are similar to the energy-harvesting efficiency, but, now the highest pitch setting shows the highest maximum efficiency. This means that for a given amount of drag, the propeller can more efficiently create negative power at a high pitch setting. The point of maximum turbine efficiency is achieved at a different advance ratio than the maximum energy-harvesting efficiency. In terms of aircraft design, it would be useful to know how much power can be extracted as a function of the allowable negative thrust. The energy-harvesting efficiency as function of (negative) T_C is shown in Fig. 14b. For a fixed allowable negative thrust, the pitch setting can be found at which the propeller harvests the most power. For example, if the vertical line at T_C=-0.05 is followed, the conclusion can be drawn that operating the propeller at $\beta_{0.7R} = 25°$ during the energy-harvesting mode actually leads to a higher extracted power than at $\beta_{0.7R} = 20°$. So even though the maximum energy-harvesting efficiency itself is higher at the low pitch setting, the associated negative thrust is also higher, reducing the turbine efficiency. Note that using the optimal η_{eh} during energy-harvesting does not necessarily mean the most harvested energy. If, for example, a lower negative T_C is chosen for the descent, the propeller has to operate at a lower energy-harvesting efficiency, but perhaps in the end, harvests more total energy, due to a longer descent time compared to a higher negative T_C.

B. Total Pressure Distribution

To increase the understanding of the flow phenomena that drive the propeller performance, especially in the energy-harvesting regime, the 5-hole pressure probe was used to analyze the total pressure distribution in the slipstream. The total pressure is expressed using the total pressure coefficient, which is different than the one defined for the 5-hole probe calibration procedure (Eq. 3). It is defined as the following:

$$C_{p_t} = \frac{p_t - p_{t_\infty}}{q_\infty} \tag{8}$$

where p_{t_∞} is determined using the pitot-tube at the front of the test section and q_∞ is determined using the tunnel calibration. The value of the total pressure coefficient should go to zero in the free stream away from the model.

1. Slipstream Uniformity

As mentioned in Sec. II.B.2, the 5-hole probe was also used to assess the uniformity of the slipstream. Two radial planes, perpendicular to the free stream, were analyzed, as can be seen in Fig. 6b, for the pitch settings of $\beta_{0.7R} = 15°$ and 30°. Only one advance ratio was chosen for this analysis, namely the one close to the maximum energy-harvesting efficiency condition. The results can be seen in Fig. 15, in which the two streamwise planes are combined into a single graph. On the left side of each graph, the pressure data of the analysis plane closest to the rotational plane are presented, while on the right, the pressure data of the analysis plane more downstream are shown. Note that in reality, the two planes were both measured on the same side of the propeller.

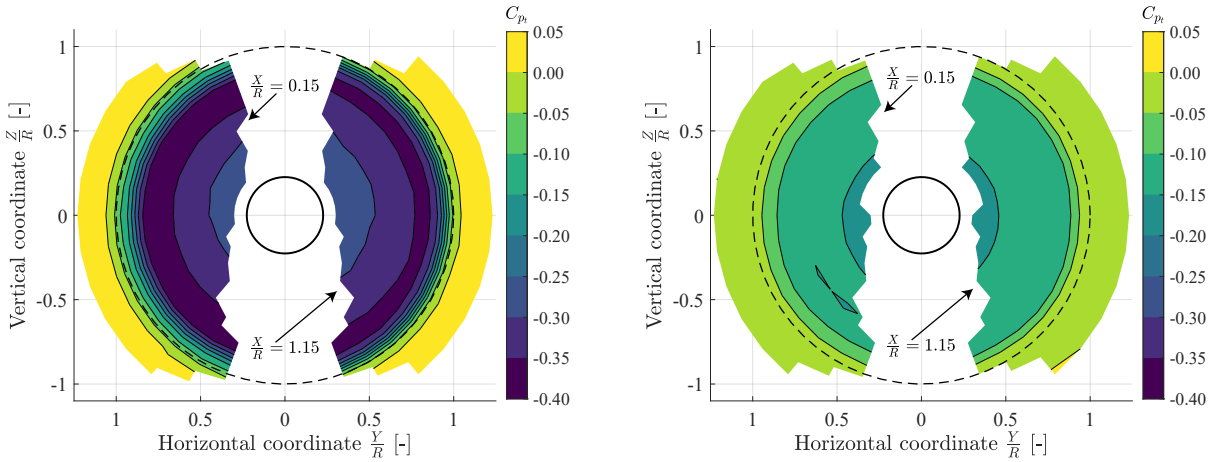

(a) $\beta_{0.7R}$=15° (J = 1.10) **(b) $\beta_{0.7R}$=30° (J = 1.90)**

Fig. 15 Total pressure coefficient distributions at the two radial planes downstream of the propeller plane close to the maximum energy-harvesting conditions

Downloaded by TU DELFT on August 16, 2022 | http://arc.aiaa.org | DOI: 10.2514/6.2022-3893

It can be seen that the slipstream looks rather uniform for the two pitch settings. Only for $\beta_{0.7R} = 30°$, there are some small deviations visible in the lower half of the analysis plane. This is also due to the discrete number of contours used for the graph. The observed uniformity shows that the single horizontal plane can be used to describe the flowfield in the entire slipstream.

2. Blade Loading

The total pressure distribution close to the propeller plane is indicative of the radial distribution of blade loading. In Fig. 16 the total pressure distributions obtained using the 5-hole probe are presented for the two pitch settings that were analyzed. These distributions were obtained at $0.15R$ downstream of the propeller plane. For $\beta_{0.7R} = 15°$, the results are shown for $J = 0.60$, $J = 0.75$, and $J = 1.10$ in Fig. 16a. These advance ratios were expected to be representative of the maximum propeller efficiency in the propulsive mode, the zero thrust condition, and the maximum energy-harvesting power output, but the measurements showed that those points actually occurred at slightly different J. For $\beta_{0.7R} = 15°$, the total pressure distribution for the propulsive condition shows that the tip region is already negatively loaded. This is due to the local negative angles of attack, meaning this blade pitch setting can not yield a high propeller efficiency. For the zero thrust conditions, the inboard part, with exception of the root part, has a positive loading, while the whole outboard region, from 70% of the blade radius on, is negatively loaded, resulting in a close to zero net loading. For the energy-harvesting mode, the total pressure distribution is rather flat over a large part of the blade span, indicating that the blade sections are operating at sub-optimal performance. Numerical simulations performed by Goyal et al. [10] have shown that almost the complete blade has actually stalled at these energy-harvesting conditions, confirming the flat loading distribution observed.

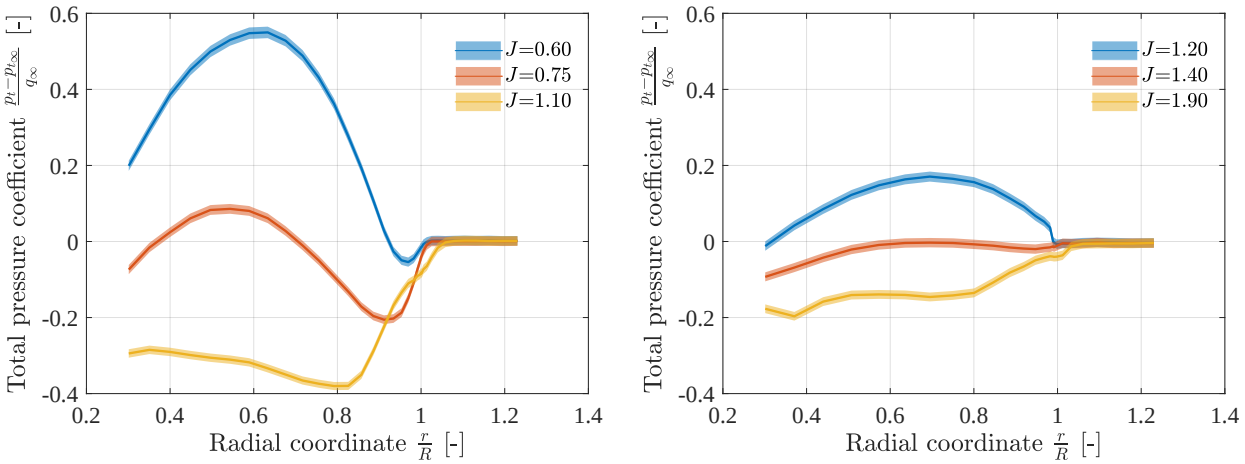

(a) $\beta_{0.7R}$=15° **(b) $\beta_{0.7R}$=30°**

Fig. 16 Total pressure coefficient distributions at $0.15R$ downstream of the propeller plane

In Fig. 16b, the results are shown for $\beta_{0.7R} = 30°$. For this blade pitch, there was a bigger mismatch between the predicted and actual advance ratios at which the three mentioned conditions were obtained, which is most apparent in the zero thrust case ($J = 1.40$), where almost the whole blade shows a negative loading, even though this loading is very small. The propulsive mode ($J = 1.20$) shows a positive total pressure distribution over the whole blade, indicating that the tip region is not negatively loaded, as was the case at the lower pitch setting, resulting in a higher propeller efficiency. It can also be observed that this maximum propulsive efficiency is indeed obtained at a lower blade loading, resulting in less profile and induction losses. Also, the absolute forces are smaller due to the lower rotational speed. In the energy-harvesting mode ($J = 1.90$), there is again a flat total pressure distribution, even more than at the lower pitch setting. This indicates that the blade sections have even a worse performance compared to $\beta_{0.7R} = 15°$, lowering the energy-harvesting efficiency.

Downloaded by TU DELFT on August 16, 2022 | http://arc.aiaa.org | DOI: 10.2514/6.2022-3893

Downloaded by TU DELFT on August 16, 2022 | http://arc.aiaa.org | DOI: 10.2514/6.2022-3893

C. Slipstream Induced Velocities

To analyze the slipstream velocity distributions, both phase-locked and phase-averaged PIV was performed. The PIV was done for $\beta_{0.7R} = 15°$ and $\beta_{0.7R} = 30°$, at the same three advance ratios for which the 5-hole probe measurements were performed. In this way, the results from the two different methods could be compared. For the discussion of the PIV results, the propulsive and the energy-harvesting mode were considered, while the zero-thrust case was left out. The free stream velocity was fixed to 30 m/s and the advance ratio was changed by varying the rotational speed. The total analysis plane was measured in two steps by traversing the PIV system. The two separate fields were combined in the post-processing. In Sec. III.C.2 the phase-averaged results are discussed and in Sec. III.C.2, the phase-locked results are presented. The part of the slipstream velocity fields around the propeller blades was removed since no accurate correlations could be found here. Furthermore, part of the velocity field close to the nacelle was removed, since the reflection of the laser made it impossible to identify the particles in that region.

1. Phase-averaged Velocity Field

The slipstream flowfields obtained by the phase-averaged PIV results give insight into the inflow to a downstream element positioned inside the slipstream. This experiment did not feature an installed configuration, but the lifting surfaces behind the propeller, which are partially submerged in the slipstream, will see an altered performance. The data for $\beta_{0.7R} = 15°$ are presented in Fig. 17. As mentioned in Sec. II.B.3, 2000 image pairs were acquired for each advance ratio. The propulsive mode shows an increase in axial velocity in the slipstream, see Fig. 17a, similar to the observed trend in total pressure. Behind the tip, there is a small region of expanding flow associated with the outboard negative loading, while the positively loaded part of the blade shows a contracting slipstream behind it.

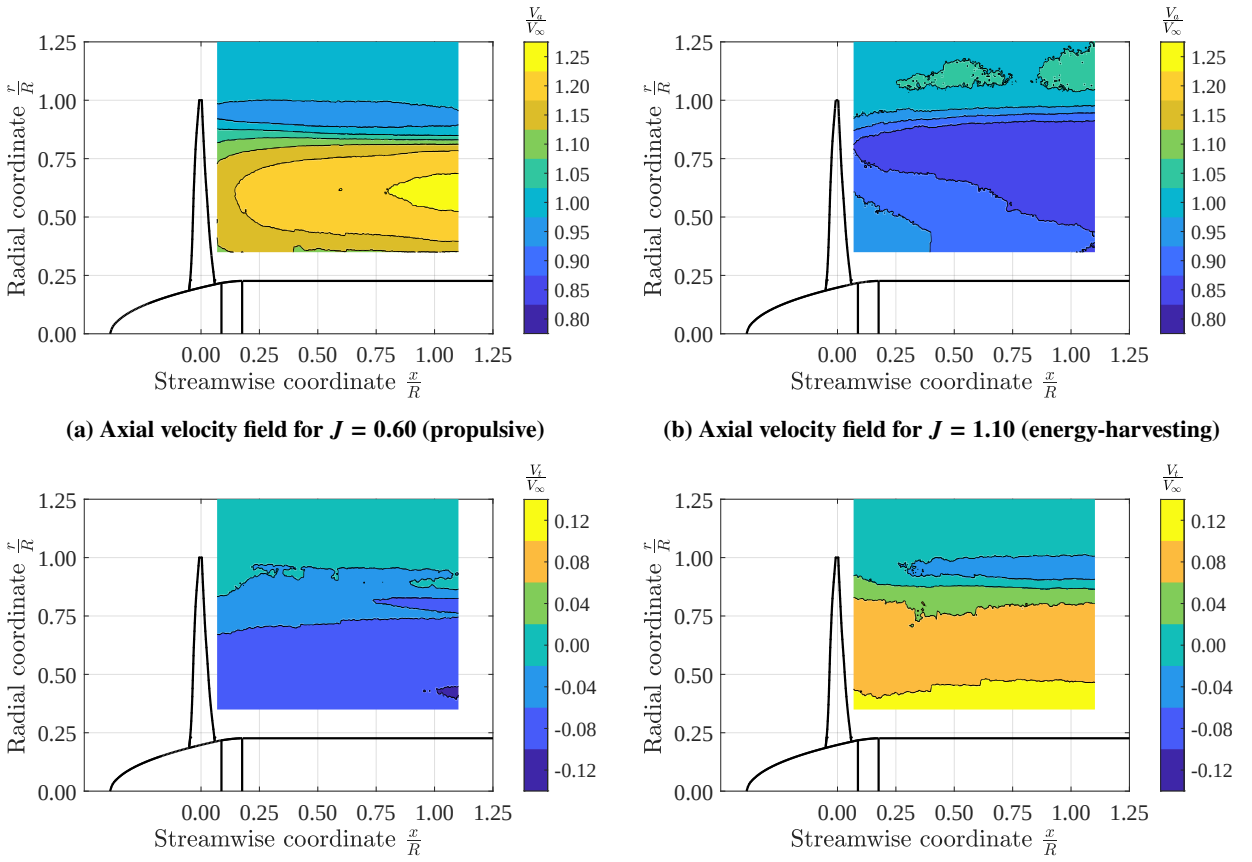

(a) Axial velocity field for $J = 0.60$ (propulsive)

(b) Axial velocity field for $J = 1.10$ (energy-harvesting)

(c) Tangential velocity field for $J = 0.60$ (propulsive)

(d) Tangential velocity field for $J = 1.10$ (energy-harvesting)

Fig. 17 Phase-averaged velocity fields in the propeller slipstream for $\beta_{0.7R}$=15° showing axial and tangential (swirl) velocity

Note that the propeller was rotating into the plane, meaning the swirl component in the propulsive mode is negative, see Fig. 17c. However, for the energy-harvesting, the negative torque on the blade sections results in an opposite swirl component, hence a positive sign, meaning the slipstream is rotating in the opposite direction, see Fig. 17d. The swirl distribution for the propulsive case is rather flat, which is normal for the propulsive mode [8]. For the energy-harvesting mode, there is clearly a reduction in axial velocity (Fig. 17b), which would yield a reduction in lift of any lifting surface submerged into the slipstream. The largest reduction in axial velocity is found at the location where the highest negative loading was observed. The variations observed in the free stream in Fig. 17b were due to the measurement uncertainty in combination with the chosen contour levels. The tangential velocity in the energy-harvesting mode (Fig. 17d) is largest near the root and becomes smaller towards the tip. The change in swirl direction will also invert the swirl effects on a lifting surface behind the propeller. This can be disadvantageous for wing-mounted propellers, where the swirl recovery may become less beneficial. For $\beta_{0.7R} = 30°$ the results were similar except for the propulsive mode for which the whole slipstream was accelerated with respect to the freestream.

2. Phase-locked

To further compare the observed integral performance and total pressure distribution just behind the propeller blades, phase-locked PIV was performed. Furthermore, the phase-locked velocity fields explain the observed phase-averaged behavior. As mentioned in Sec. II.B.3, 500 image pairs were acquired for each advance ratio, synchronized with the rotational speed of the propeller. The data for $\beta_{0.7R} = 15°$ are presented in Fig. 18. The axial velocity fields are shown in Fig. 18a and Fig. 18b for the propulsive mode ($J = 0.60$) and the energy-harvesting mode ($J = 1.10$) respectively. The tangential (swirl) velocity fields are shown in Fig. 18c and Fig. 18d for the propulsive mode ($J = 0.60$) and the energy-harvesting mode ($J = 1.10$) respectively.

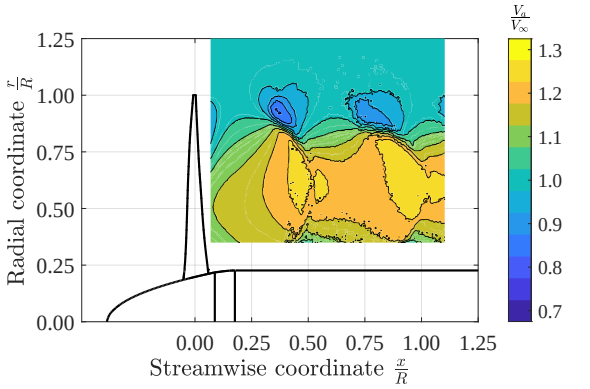

(a) Axial velocity field for $J = 0.60$ (propulsive)

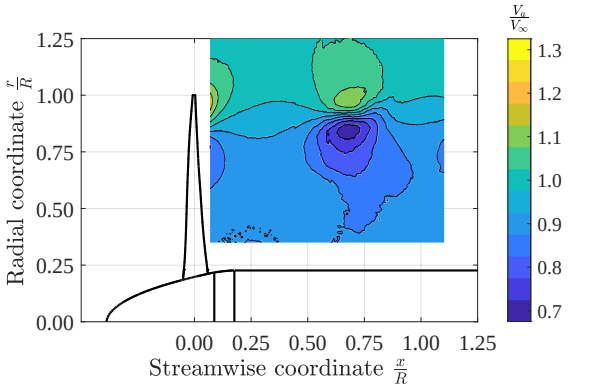

(b) Axial velocity field for $J = 1.10$ (energy-harvesting)

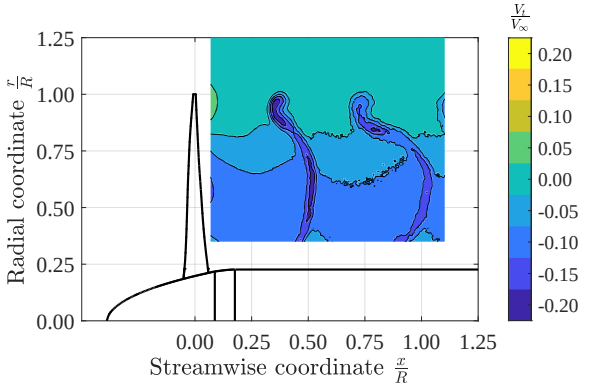

(c) Tangential velocity field for $J = 0.60$ (propulsive)

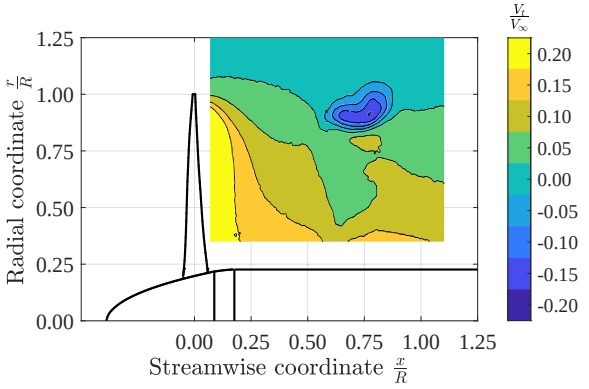

(d) Tangential velocity field for $J = 1.10$ (energy-harvesting)

Fig. 18 Phase-locked velocity fields in the propeller slipstream for $\beta_{0.7R}$=15° showing axial and tangential (swirl) velocity

Downloaded by TU DELFT on August 16, 2022 | http://arc.aiaa.org | DOI: 10.2514/6.2022-3893

For the propulsive mode, see Fig. 18a and Fig. 18c, the blade wake is clearly visible, both in terms of axial and tangential velocity. Strong gradients are introduced by the blade wakes and the tip vortices. The negative tip loading observed in the total pressure data is also being recognized in the velocity fields. For a regular propulsive operating condition, the loading would be positive over the entire blade span and hence a single tip vortex would be positioned at the edge of the slipstream. However, due to the negative loading at the tip for this low pitch setting, the strongest trailing vortex is located more inboard. In the energy-harvesting mode, the wake of the blades is much less clearly defined than for the propulsive case, which is due to the lower velocity gradients in the slipstream compared to the propulsive mode, which was also observed in the total pressure data. However, the tangential velocity field for the energy-harvesting mode (Fig. 18d) does show large gradients right behind the blade.

The same velocity fields, but for $\beta_{0.7R} = 30°$, are shown in Fig. 19. Here the maximum propeller efficiency in the propulsive mode was reached around $J = 1.20$, while the maximum energy-harvesting efficiency was obtained at around $J = 1.90$. Note that the tangential velocity fields for$\beta_{0.7R} = 30°$ for both thrust settings show patchy behavior, which was due to the rather low velocity values in combination with the in-plane uncertainty. The results show similar trends compared to the low pitch setting. In the propulsive mode, the blade wake and tip vortex are clearly visible due to the large velocity gradients, both in terms of axial and tangential velocity (Fig. 19a and Fig. 19c). For the energy-harvesting mode, the rotational speed was even lower, and hence the blade wake was not fully captured in the total field-of-view. Similar to $\beta_{0.7R} = 15°$, the swirl in the slipstream for the energy-harvesting mode (Fig. 19b and Fig. 19d) is not showing a well-defined blade wake. The not well-defined blade wake in the energy-harvesting mode for both pitch settings makes the slipstream more chaotic than for the propulsive mode. This is probably caused by the stall on the blade sections in the energy-harvesting mode, leading to unsteady pressure fluctuations. The increased unsteadiness of the slipstream and the sub-optimal blade loading can also lead to more vibration of the propeller and structures submerged in the slipstream, possibly resulting in an increased structureborne noise.

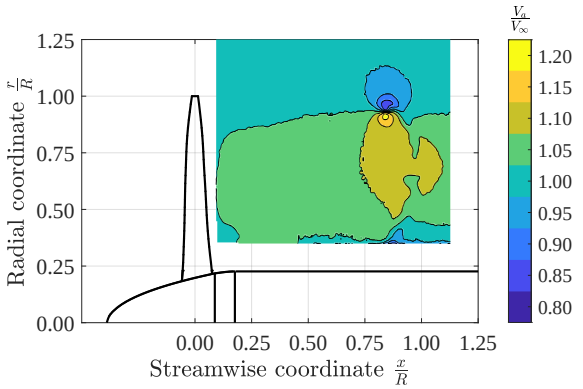

(a) Axial velocity field for $J = 1.20$ (propulsive)

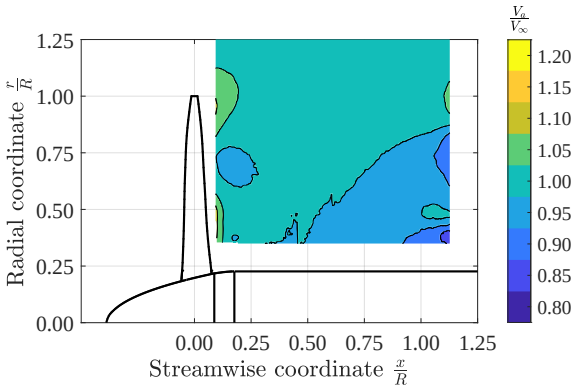

(b) Axial velocity field for $J = 1.90$ (energy-harvesting)

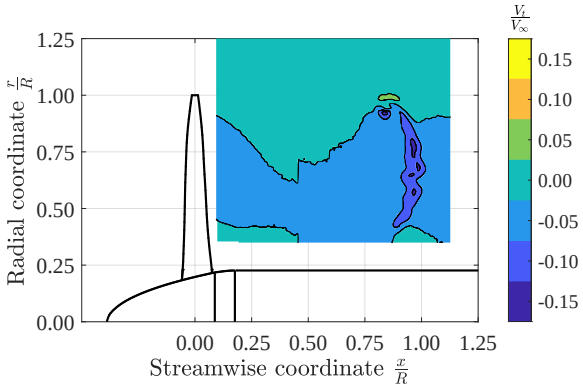

(c) Tangential velocity field for $J = 1.20$ (propulsive)

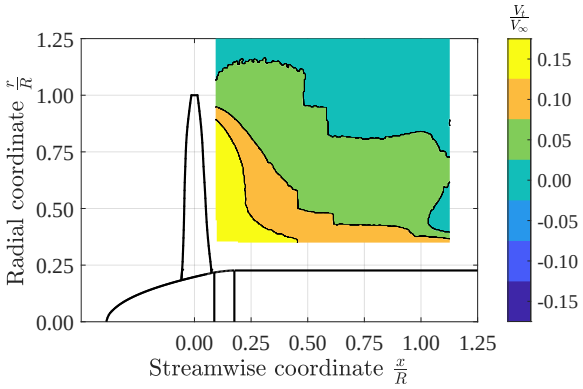

(d) Tangential velocity field for $J = 1.90$ (energy-harvesting)

Fig. 19 Phase-locked velocity fields in the propeller slipstream for $\beta_{0.7R}$=30° showing axial and tangential (swirl) velocity

Downloaded by TU DELFT on August 16, 2022 | http://arc.aiaa.org | DOI: 10.2514/6.2022-3893

IV. Conclusions

This paper has quantified the aerodynamic performance of a three-bladed propeller that was operated at both positive and negative thrust and power conditions. The propeller was tested in the Low-Turbulence Tunnel at Delft University of Technology. Based on the results, the following conclusions were drawn:

- In the energy-harvesting regime, the thrust and power coefficient flatten due to the increased negative angles of attack on the blade sections, since this propeller is not designed for energy-harvesting operations. The highly cambered blade sections are prone to separation in the energy-harvesting mode, limiting the performance.
- The energy harvesting efficiency was found to be optimal in between a pitch setting of $\beta_{0.7R} = 10°$ and $\beta_{0.7R} = 15°$, since both showed a similar maximum. The maximum energy-harvesting efficiency was still limited to around 11%, which is rather low compared to equivalent wind turbines. Increasing the pitch setting reduces this energy-harvesting efficiency even further, where $\beta_{0.7R} = 30°$ only showed a 6% maximum efficiency in the energy-harvesting mode.
- For a fixed free stream velocity, a low pitch setting shows a smaller negative C_q compared to high pitch settings, since the maximum energy-harvesting condition is reached at a lower advance ratio and hence inflow angle. This means that for the low pitch setting, the lift vector is contributing less to the negative power coefficient. Due to the higher rotational speed at which the low pitch setting has its maximum energy-harvesting efficiency, the total output power is large.
- The large energy-harvesting efficiency at low pitch settings comes at a cost of increased negative thrust. The turbine efficiency at these low pitch settings, which is a measure of the propeller's ability to convert negative loading into output power, is lower than for the high pitch settings. Increasing the pitch setting leads to an increasingly higher turbine efficiency, although this means lowering the maximum energy-harvesting efficiency. For low values of allowable negative thrust, the most power can actually be harvested by using a high pitch setting.
- Increasing the Reynolds and Mach number by increasing the free stream velocity yields higher performance in both the propulsive and energy-harvesting mode for a given advance ratio.
- The total pressure distribution behind the blades showed small gradients of the radial loading distribution for the energy-harvesting conditions compared to the propulsive conditions, for both examined pitch settings. This indicates that the blade sections are close to stall conditions, which impacts the energy-harvesting performance.
- The phase-locked PIV showed a distinctive blade wake and tip vortex for the propulsive mode. However, the velocity gradients in the slipstream for the energy-harvesting mode are lower and the blade wake is, therefore, less apparent. This results in more spread out unsteady pressure fluctuations in the slipstream.
- For a surface submerged in the slipstream of an energy-harvesting propeller, the induced velocity in the slipstream will be inverted compared to the propulsive mode, meaning a reduction in axial velocity and an opposite swirl. Therefore, the position and rotation direction of an energy-harvesting propeller is of importance in the aircraft design, since the induced velocities could be detrimental to the wing performance.

The results obtained in this paper increase the knowledge of the operation of propellers that operate in negative thrust conditions. In this paper, the focus was put on the energy-harvesting performance, but operating a propeller in negative thrust conditions can also be done to improve control and stability or the propeller could be used as an alternative airbrake. The use of propellers to harvest energy in the descent phase could lead to a reduction in the total energy consumption of aircraft, hence reducing the adverse impact of their operation on the environment.

Downloaded by TU DELFT on August 16, 2022 | http://arc.aiaa.org | DOI: 10.2514/6.2022-3893

Acknowledgments

The research leading to these results is part of the FUTPRINT50 project. This project has received funding from the European Union's Horizon 2020 Research and Innovation programme under Grant Agreement No 875551.

References

[1] M. Hepperle, "*Electric Flight - Potential and Limitations*," Avt-209 workshop, DLR, 2012.

[2] M. D. Moore and B. Fredericks, "Misconceptions of Electric Propulsion Aircraft and their Emergent Aviation Markets," *AIAA Paper 2014-0535*, Vol. 52nd Aerospace Sciences Meeting, 2014. https://doi.org/10.2514/6.2014-0535.

[3] N. K. Borer, M. D. Patterson, J. K. Viken, M. D. Moore, S. Clarke, M. E. Redifer, R. J. Christie, A. M. Stoll, A. Dubois, J. Bevirt, A. R. Gibson, T. J. Foster and P. G. Osterkamp, "*Design and Performance of the NASA SCEPTOR Distributed Electric Propulsion Flight Demonstrator*," *AIAA AVIATION;*, Vol. 16th AIAA Aviation Technology, Integration, and Operations Conference, 2016. https://doi.org/10.2514/6.2016-3920, Washington, D.C.

[4] M. D. Patterson, J. M. Derlaga and N. K. Borer, "*High-Lift Propeller System Configuration Selection for NASA's SCEPTOR Distributed Electric Propulsion Flight Demonstrator*," *AIAA SciTech Forum;*, Vol. 16th AIAA Aviation Technology, Integration, and Operations Conference, 2016. https://doi.org/10.2514/6.2016-3922, Washington, D.C.

[5] T. Sinnige, N. van Arnhem, T. C. A. Stokkermans, G. Eitelberg and L. L. M. Veldhuis, "*Wingtip-Mounted Propellers: Aerodynamic Analysis of Interaction Effects and Comparison with Conventional Layout*," *Journal of Aircraft*, Vol. 56, No. 1, 2019, pp. 295–312. https://doi.org/10.2514/1.C034978.

[6] J. P. Barnes, "*Regenerative Electric Flight: Synergy and Integration of Dual-role Machines*," *AIAA SciTech Forum;*, Vol. 53rd AIAA Aerospace Sciences Meeting, 2015. https://doi.org/10.2514/6.2015-1302, Kissimmee, Florida.

[7] D. Eržen, M. Andrejašič, R. Lapuh, J. Tomažič, Č. Gorup, T. Kosel, "*An Optimal Propeller Design for In-flight Power Recuperation on an Electric Aircraft*," *Aviation Technology, Integration, and Operations Conference*, 2018. https://doi.org/10.2514/6.2018-3206, Atlanta, Georgia.

[8] T. Sinnige, T. C. A. Stokkermans, N. van Arnhem, L. L. M. Veldhuis, "Aerodynamic Performance of a Wingtip-Mounted Tractor Propeller Configuration in Windmilling and Energy-Harvesting Conditions," *AIAA Aviation Forum*, 2019. https://doi.org/10.2514/6.2019-3033, Dellas, Texas.

[9] F. L. Galvão, "*A Note on Glider Electric Propulsion*," *Technical Soaring*, Vol. 36, No. 4, 2012, pp. 94–101.

[10] J. Goyal, T. Sinnige, F. Avallone and C. Ferreira, "*Aerodynamic and Aeroacoustic Characteristics of an Isolated Propeller at Positive and Negative Thrust*," *AIAA AVIATION Forum;*, 2021. https://doi.org/10.2514/6.2021-2187.

[11] L. L. M. Veldhuis, "Propeller Wing Aerodynamic Interference," Ph.D. thesis, Faculty of Aerospace Engineering, Delft University of Technology, Delft, The Netherlands, 2005.

[12] T. Sinnige, "Aerodynamic and Aeroacoustic Interaction Effects for Tip-Mounted Propellers: An Experimental Study," Ph.D. thesis, Faculty of Aerospace Engineering, Delft University of Technology, Delft, The Netherlands, 2018.

Downloaded by TU DELFT on August 16, 2022 | http://arc.aiaa.org | DOI: 10.2514/6.2022-3893